Chemical Science

Accepted Manuscript

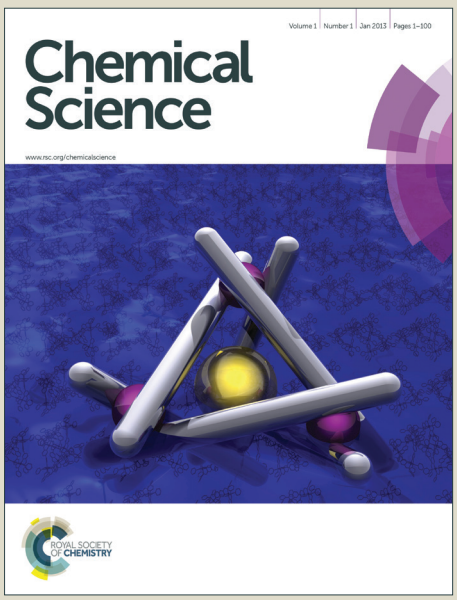

ROYAL SOCIETY OF CHEMISTRY

www.rsc.org/chemicalscience

Cite this: DOI: 10.1039/c0xx00000x

www.rsc.org/xxxxxx

ARTICLE TYPE

Charge Transfer Interactions in Self-Assembled Single Walled Carbon Nanotubes/Dawson-Wells Polyoxometalate Hybrids

Concha Bosch-Navarro,[a] Benjamin Matt,[b] Guillaume Izzet,[b] Carlos Romero-Nieto,[c,‡] Konstantin Dirian,[c] Andrés Raya,[d] Sergio I. Molina,[d] Anna Proust,[b,*] Dirk M. Guldi,[c,*] Carlos Martí-Gastaldo,[a,*] Eugenio Coronado.[a,*]

Received (in XXX, XXX) Xth XXXXXXXXX 20XX, Accepted Xth XXXXXXXXX 20XX
DOI: 10.1039/b000000x

We demonstrate the success in self-assembling pyrene-modified Dawson Wells-type polyoxometalates (POM) with single wall carbon nanotubes (SWCNT) by means of π-π interactions. In this context, the immobilization of POMs onto SWCNTs is corroborated by aberration-corrected high-resolution electron microscopy, thermogravimetric analysis, and Raman spectroscopy. From steady-state and time-resolved photophysical techniques we derived evidence for mutual interactions between SWCNTs and POMs in the excited states. The latter are the inception to a charge transfer from the SWCNTs to the POMs. Our results corroborate the suitability of POM-SWCNTs assemblies for photoactive molecular devices.

Introduction.

Tailoring hybrid nanostructures offers substantial advantages over the use of "classic" bulk solids as their use as building-blocks may permit downscaling the costs associated with more conventional technologies.[1] Moreover, nanostructure design enables integrating molecular and bulk electronic structures into sophisticated architectures with variable degree of complexity. The latter can be processed more easily and allows fine-tuning of the chemical and physical properties that arise at the nanoscale. In the context of nanoelectronics, single wall carbon nanotubes (SWCNTs) have emerged as ideal one-dimensional wires on account of their unique electronic features, large specific surface areas, high mechanical strength, and remarkable chemical robustness.[2] Hence, they have been implemented into practical devices in the areas of spintronics,[3] optoelectronics,[4] energy storage,[5] field-effect transistors (FETs)[6] or sensors.[7]

Polyoxometalates (POMs) are an archetypical family of inorganic polynuclear metal-oxo nanoclusters.[8] Their unmatched structural versatilities provide accessible chemical means to modulate their electronic behavior. This results in a rich landscape of magnetic, catalytic, and redox properties, which, alongside their chemical robustness, are currently attracting particular interest in areas like molecular magnetism,[9] molecular spintronics,[10] and water oxidation catalysis.[11]

This interest has now evolved into the creation of SWCNT-POM hybrid architectures by immobilizing electronically active POMs to the sidewalls of carbon nanotubes by means of either covalent or non-covalent interactions. For example, Chen *et al*. reported the grafting of the Keggin-type $H_7PMo_{12}O_{42}$ onto SWCNTs and the use of the resulting assemblies as a catalyst support for the better dispersion of electrocatalytic nanoparticles.[12] Mialane *et al.* succeeded in isolating magnetic hybrids by incorporating magnetic POMs like $[Fe_4(H_2O)_2(FeW_9O_{34})_2]^{10-}$ or $[As_2W_{20}O_{68}Co(H_2O)]^{8-}$ and suggested that the magnetic response of the clusters was retained after their grafting.[13] More recent reports illustrate the potential benefits of these assemblies in catalysis[14] or molecular cluster batteries.[15] Whilst these precedents solely explored simple chemisorption or electrostatic trapping of the POMs to immobilize them on the surface of the chemically unmodified nanotubes, there are also abundant examples of organic/inorganic POM-based hybrids assembled from covalent post-functionalization reactions of interest in artificial photosynthesis,[16] molecular self-healing[17] or molecular electronics.[18,19] The covalent approach renders stronger interactions between the organic and the inorganic components besides better control over the structure of the hybrids.[20]

Although covalent or electrostatic interactions provide strong SWCNT-POM coupling, they also affect the electronic properties of the nanotubes as result of the introduction of defects to the original sp^2 structure.[21] Supramolecular π-π grafting affords a strong contact within the carbon-based hybrids, whilst leaving the electronic properties of SWCNTs intact, featuring as the best choice for the fabrication of photoactive assemblies. In particular, Pyrene (Pyr) and pyr derivatives enable strong interactions within carbon-based hybrids without affecting the electronic properties of SWCNTs, including ballistic conductance and optical transitions. Previous studies have demonstrated the versatility of this polyaromatic hydrocarbon to facilitate the grafting of a wide variety of molecular building blocks like redox-active transition metal complexes,[22] single molecule magnets,[23] phthalocyanines,[24] quantum dots,[25] and even DNA to the sidewalls of SWCNTs.[26]

Built upon these considerations, the use of POMs derivatized with pyr as anchoring groups could give rise to stable hybrids, whose stability might be further increased by a nanotweezer-like geometry (*i.e.* when two or more aromatic units are involved in the binding with the SWCNTs).[27] The strong coupling between pyr and the nanotubes' sidewalls is also favorable to study the electronic communication within the hybrid. However, non-covalent functionalization of SWCNTs with POMs has been mostly unexplored to date – only two examples have been reported –[28] likely due to the intrinsic

synthetic difficulties to chemically derivatize the POM's periphery. Among the wide array of available POMs, we targeted Dawson-Wells polyoxometalates, $[M_{18}O_{62}X_2]^{n-}$,[29] on the basis of its chemical versatility. The latter permits modifying its inorganic framework to produce non-classical or lacunary Dawson-Wells POMs[30] as well as more complex multifunctional materials and hybrids.[20]

In this work, we report the preparation, characterization and electronic communication in photoactive **SWCNT-POM** hybrids, which incorporate Dawson-Wells-type POMs bearing pendant pyrenes (**POM-pyr; Fig.1**) to enable their grafting onto SWCNTs via π-π interactions. **POM-pyr** was designed to feature a nanotweezers-like geometry that reinforces the coupling between the two anchoring pyrenes and SWCNTs to maximize the stability of the resulting hybrids.[27]

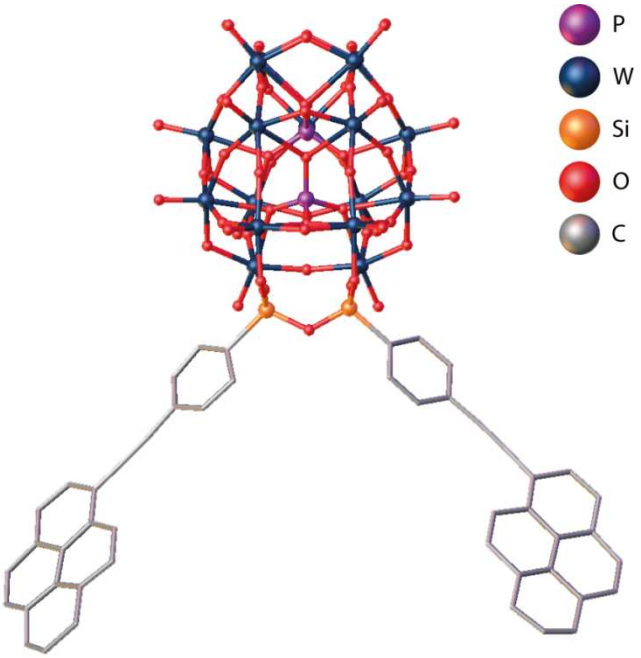

Figure 1. Structure of $[P_2W_{17}O_{61}\{O(Si\text{-}phenyl\text{-}ethynyl\text{-}pyrene)_2\}]^{6-}$ (POM-pyr).

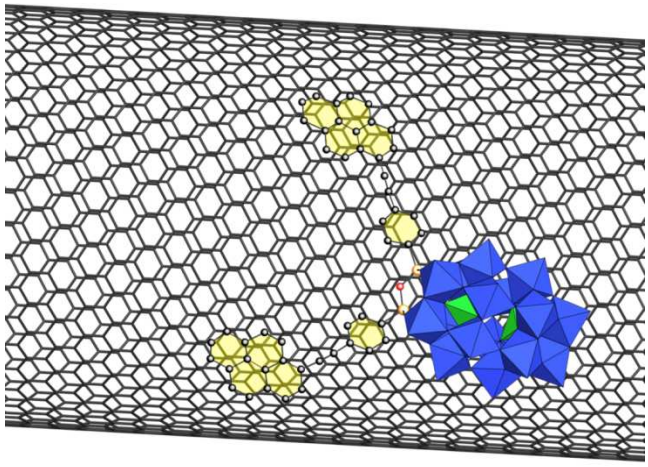

Scheme 1. SWCNT-POM formed upon assembly of POM-pyr by means of π-π stacking of the pendant pyrenes of POM-pyr onto the sidewalls of SWCNTs. Tetrabutylammonium (TBA) cations are omitted for clarity

Our photophysical investigations suggest that the use of fully conjugated organic moieties grafted to the POMs is decisive to trigger an efficient electronic communication between the different constituents, with SWCNTs and POMs acting as electron donors and acceptors, respectively. Combination of this feature with the ability of POMs to undergo multiple reductions renders the described **SWCNT-POM** hybrids as versatile electron reservoir for catalysis.

Results and discussion.

Synthesis of SWCNT-POM hybrids. The synthesis of the tetrabutylammonium salt of the pyrene-derivatized Dawson-Wells polyoxometalate $(TBA)_6[P_2W_{17}O_{61}\{O(Si\text{-}phenyl\text{-}ethynyl\text{-}pyrene)_2\}]$ (**POM-pyr; Fig.1**) was prepared as previously described by Sonogashira cross-coupling reaction of an iodo aryl POM intermediate with an alkynyl pyrene derivative.[31] The **SWCNT-POM** hybrids are prepared by adding **POM-pyr** to a fresh dispersion of commercial grade SWCNTs (*i.e.*, HiPco® and Elicarb® SWCNTs) in DMF, which is left to settle overnight (**Scheme 1**). The solid is then collected by centrifugation and filtration, followed by thorough washing with DMF and acetonitrile to ensure removal of the excess of non-grafted **POM-pyr**.

Thermogravimetric analysis (TGA). TGA was firstly used to confirm the functionalization of SWCNTs (**Fig. SI1**). Thermal decomposition of the hybrid is dominated by the nanotubes' response. Bare SWCNTs oxidize in a single, narrow process centered at 580 ºC, whereas **SWCNT-POM** displays, on one hand, in the temperature regime up to 500 ºC a thermal decomposition at 450 ºC and, on the other hand, in the temperature regime beyond 500 ºC a similar thermal stability than SWCNTs. As such, this behavior is governed by the presence of immobilized **POM-pyr**, whose organic moieties and ammonium counterions start to decompose at 350 ºC for the starting TBA salt. The latter does not exert significant damage to the SWCNT structure, which is generally associated to poorer thermal stability due to the introduction of defects.[32] According to the calculations described in **Fig. SI1**, the remaining mass of the **SWCNT-POM** hybrids with respect to the pristine SWCNTs is estimated to be close to 10% (1 **POM-pyr** unit per 4600 carbon atoms).[33]

Electron Microscopy and EDS (Energy-Dispersive X-ray Spectroscopy) Analysis. High Resolution Transmission Electron Microscopy (HRTEM) images were collected from samples prepared by dropping fresh EtOH suspensions of **SCWNT-POM** hybrids on a carbon-coated copper grid. **Fig. SI2** illustrates the presence of nanotube bundles with multiple interlocked junctions, which are mainly composed by carbon according to local EDS analysis, alongside a heterogeneous distribution of conglomerates with higher contrast composed by Si and W, consistent with the immobilization of Dawson-Wells-type POMs.

We next performed Aberration-corrected High-Angle Annular Dark-Field Scanning-Transmission Electron Microscopy (HAADF-STEM) and Bright Field (BF)-STEM to determine the positioning of the **POM-pyr** clusters along the surface of SWCNTs (**Fig. 2** & **Fig. SI3**). The major advantage of HAADF-

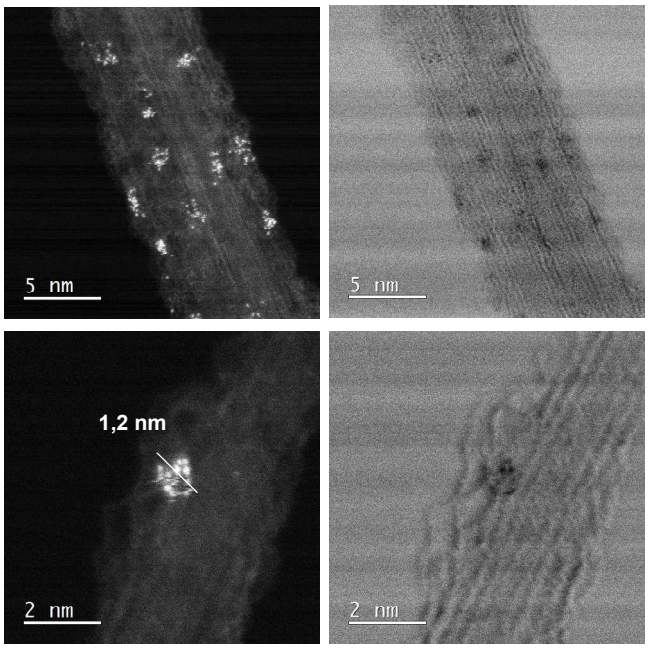

Figure 2. HAADF-STEM (*up left*) and BF-STEM (*up right*) images showing the presence of POM-pyr clusters (bright spots) along the sidewalls of SWCNTs. In the bottom image, a zoom-in is done over a bright spot, which have a size of 1.2 x 1 nm, in good agreement with the size of the POM-pyr clusters

STEM over HRTEM is the non-existence of contrast reversal with specimen thickness and microscope parameters. This is due to the incoherent nature of the HAADF-STEM image process formation. Sub-Ångstrom resolution is achieved by using aberration corrected electron microscopes and, therefore, atomic columns and even individual atoms can be imaged. The intensity in HAADF images can be correlated with the atomic number (Z) of the present elements. Hence, elements with a high Z such as tungsten (W; Z=74) show high contrast, whereas lighter elements like carbon (C; Z=6) are hardly discernable. HAADF-STEM in **Fig. 2** displays the presence of bright spots decorating the sidewalls of SWCNTs. These bright spots correspond to the projection of the structure formed by the W atoms of POMs. However, it remains difficult to establish exact atom-by-atom correlation between the observed projection and the structure of **POM-pyr**. The following aspects need careful consideration. On one hand, from analyzing just a single image we cannot differentiate between a bright spot that corresponds to a single atom or to two atoms, which are aligned or partially overlapped in the direction of the optical axis. On the other hand, several orientations of the **SWCNT-POM** hybrids may result in similar projections relative to the plane perpendicular to the incident electron beam.

Electron tomography experiments could not be performed because of the instability of the POM structure caused by the interaction with the electron beam. Besides, SWCNTs are more easily distinguished in the BF image (**Fig. 2,** right). The latter confirms the heterogeneous distribution of objects along SWCNTs composed of species with heavy atoms and with sizes of approximately 1.2 nm, in excellent agreement with the dimensions of the Dawson-Wells-type POMs.

X-Ray Photoelectron Spectroscopy (XPS). XPS was also used to determine the presence of **POM-pyr** in **SWCNT-POM** hybrids and to rule out changes in its chemical nature upon immobilization. According to **Fig. 3**, the binding energies (BEs)

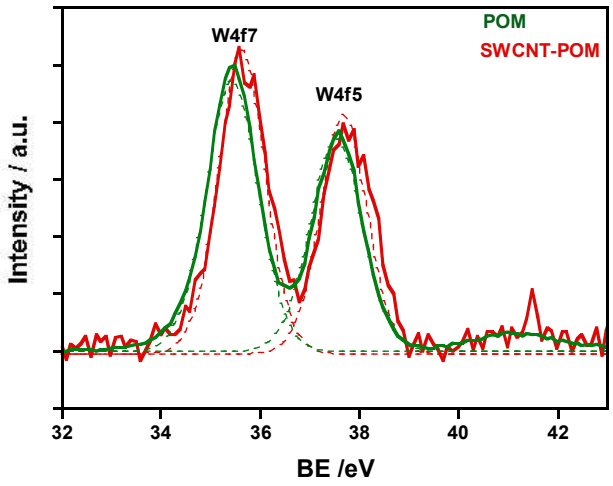

Sample	W4f (BE, eV)	
	W4f7	W4f5
POM	35.43	37.53
SWCNT@POM	35.62	37.68

Figure 3. W 4f high-resolution XPS spectra of **POM-pyr** (green spectrum) and **SWCNT-POM** (red spectrum). The dashed-lines represent the deconvolution for each sample. The binding energies (BE) extracted from the spectra are summarized in the table (*bottom*)

for the W 4f signals in the XPS spectrum of **SWCNT-POM** hybrids agree with the data collected from a crystalline sample of **POM-pyr**. Both spectra display a doublet centered at *ca.* 35 and 38 eV, with an energy splitting of approximately 2.1 eV. These peaks originate from the spin–orbit splitting into the W $4f_{5/2}$ and W $4f_{7/2}$ levels, respectively.[34] In summary, these values confirm the presence of W-O bonds in both samples and confirm the presence of intact **POM-pyr** in **SWCNT-POM** hybrids.

Physicochemical properties. Upfront we tested **POM-pyr** and its relevant references in oxidative and reductive processes – a full account is given in references 16 and 31. Given that standard electrochemical measurements, like cyclic voltammetry, etc. are reported in the aforementioned papers, we focused our investigation onto spectroelectrochemical measurements. In particular, we applied variable potentials in either the reductive or the oxidative ranges and recorded the absorption spectra in given intervals. Notably, differential spectra rather than absolute spectra are shown to illustrate the spectral changes. Thus, in **POM-pyr** the two first reduction (-0.73V and -1.14V *vs* SCE) are POM centred, while the oxidation (ca. 1.3 V *vs* SCE) involves pyr. In terms of differential absorption changes, applying a potential of +0.9 V vs. $Ag/AgNO_3$ has been shown to oxidize quasi-reversibly pyr and pyrene-1-methanol, which due its functionalization serves a reference to **POM-pyr** in the form of newly developing minima at 308, 322, and 336 nm for the earlier as well as 315, 328, and 344 nm for the latter in $TBAPF_6$ containing DMF solutions (either 0.1 or 0.2 M) (**Fig. SI4**). These are accompanied by maxima at 360, 400, 430, and 457 nm for pyr and at 362, 375 and 396 nm for pyrene-1-methanol. In the case of **POM-pyr**, where the oxidation leads to irreversible changes, a bleaching of the sharp maxima at 300, 369, and 392 nm occur, which are accompanied by broad and still defined features throughout the 400-500 nm range (**Fig. SI4**).

In contrast, when applying a potential of -0.8 V vs Ag-wire as pseudo reference electrode, discernible changes can be observed, which are related to the filling of electronic d-states, and includes a sharp and a broad maximum between 400 and 550 nm and between 600 and 1200 nm, respectively (**Fig. 4**). The

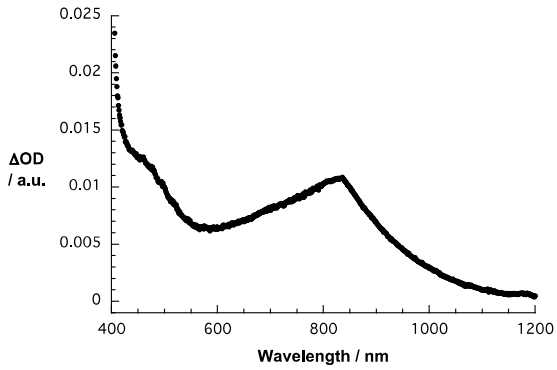

Figure 4. Differential absorption spectra (visible and near-infrared) obtained upon electrochemical reduction of **POM-pyr** in DMF with an applied potential of -0.8 V vs. Ag-wire as pseudo reference electrode.

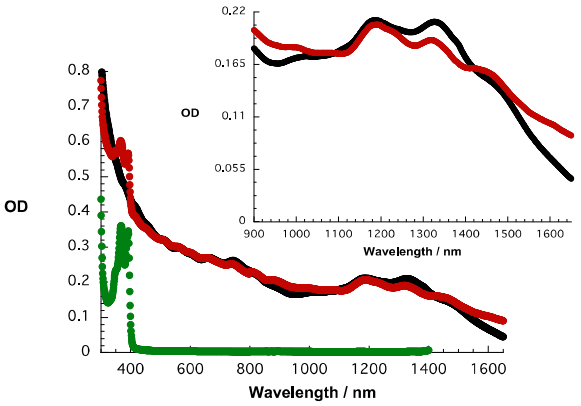

Figure 5. Absorption spectra of **SWCNT/SDBS** in D_2O (black spectrum), **SWCNT-POM** in DMF (red spectrum), and **POM-pyr** in DMF (green spectrum). Inset illustrates the near-infrared part of the absorption spectra.

corresponding maxima are noted at 450 and 830 nm. Upon applying a moderate positive potential (0.1 V), the aforementioned features retransform to those of the ground state. This trend corroborates previous cyclic voltammetric investigations in terms of the reversibility of the underlying process.

Insights into electronic communication between **POM-pyr** and SWCNTs were carefully probed by means of steady state and transient absorption assays. DMF suspensions of **SWCNT-POM** hybrids were initially tested by absorption spectroscopy and compared to the response of bare SWCNTs, which were suspended with sodium dodecyl benzene sulfonate (SWCNT/SDBS) in D_2O. Here, two types of SWCNTs, namely HiPco® and Elicarb® SWCNTs, stood at the forefront of the investigations. Owing, however, to the lack of notable absorption / fluorescence features for Elicarb® SWCNTs in the NIR – either in the form of **SWCNT-POM** hybrids or SWCNT/SDBS – we focused our investigations on HiPco SWCNTs. A close look at the absorption spectra of HiPco **SWCNT-POM** in DMF and HiPco SWCNT/SDBS in D_2O reveals M_{11}, E_{22}, and E_{11} absorption peaks at 420, 450, 510, 560, 600, 660, 740, 1010, 1190, 1325, and 1450 nm (**Fig. 5**).[35,37] The absence of appreciable shifts, which are also seen in the absence of **POM-pyr**, between the earlier and the latter, leads us to rule out the presence of electronic interactions in the ground state of HiPco **SWCNT-POM** hybrids. Previous studies have revealed red shifts of up to 30 nm.[38] It is worthwhile highlighting that DMF solutions of **POM-pyr** present a shoulder at 350 nm and maxima at 368 and 392 nm in their absorption spectra. Similarly, the absorption spectrum of HiPco **SWCNT-POM** displays maxima at 350, 368 and 390 nm, which are, therefore, attributed to the presence of **POM-pyr** that are immobilized onto HiPco.

Next, the fluorescence features of HiPco SWCNT/SDBS and HiPco **SWCNT-POM** hybrids were investigated. In particular, HiPco **SWCNT-POM** display E_{11} fluorescence maxima at 1076, 1127, 1212, 1295 and 1437 nm – (10,2), (9,4), (8,6), (8,7) and (9,7) SWCNTs – when exciting at 650 nm (**Fig. 6**). Owing to the fact that the fluorescent features of HiPco **SWCNT-POM** hybrids mirror image the corresponding

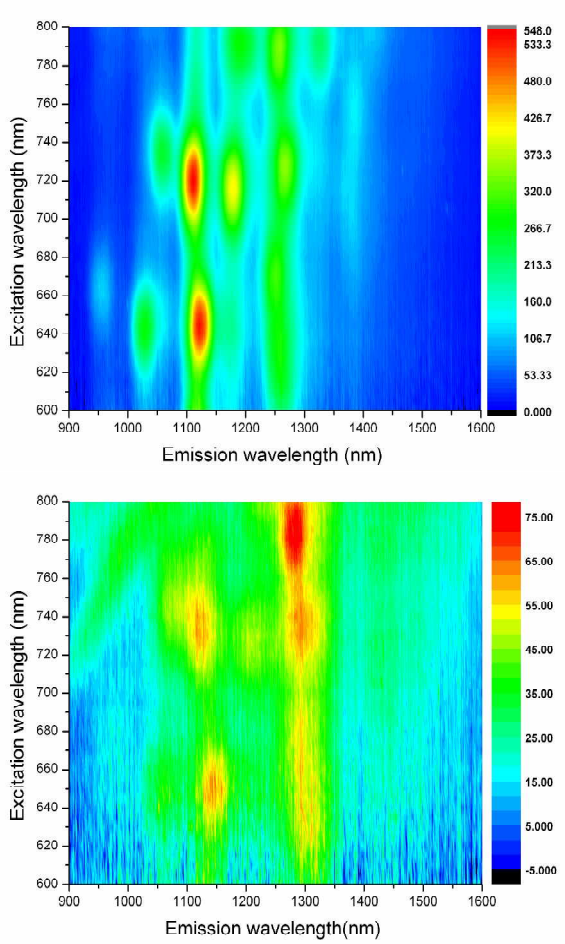

Figure 6. (*Top*) 3D steady-state NIR fluorescence spectrum with increasing intensity from blue to green to yellow and to red of SWCNT/SDBS in D_2O. (*Bottom*) 3D steady-state NIR fluorescence spectrum with increasing intensity from blue to green to yellow and to red of **SWCNT-POM** in DMF.

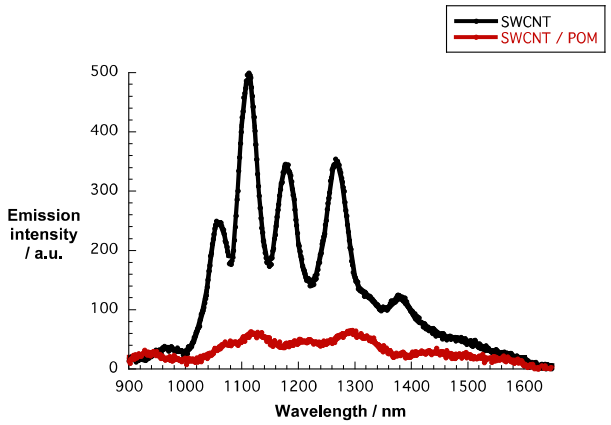

Figure 7. Comparison of the NIR fluorescence spectra of SWCNT/SDBS (black spectrum) in D_2O and **SWCNT-POM** (red spectrum) in DMF – 650 nm excitation.

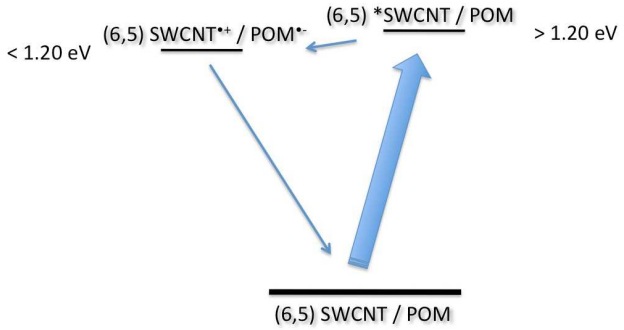

Figure 8. Energy diagram illustrating the charge separation evolving from photoexcited SWCNTs - exemplified for (6,5) SWCNT- to POM and subsequent charge recombination in competition to radiative and non-radiative (not shown) deactivation.

ground state absorption, we associate both processes to the fundamental transitions across the band gap. Contrasting the fluorescence of the **SWCNT-POM** hybrids with that of SWCNT/SDBS at equal absorbances at the excitation wavelength sheds light onto the mutual interactions via either radiative or non-radiative decays in the **SWCNT-POM** hybrids (**Fig. 6**). To this end, HiPco **SWCNT-POM** hybrids reveal an energetic shift of the fluorescent transitions in the form of red-shifted maxima relative to those seen for HiPco SWCNT/SDBS. For HiPco SWCNT/SDBS, maxima at 1054, 1113, 1174, 1268, and 1376 nm were measured, which correspond to (10,2), (9,4), (8,6), (8,7) and (9,7) SWCNTs, respectively.[37]

We rationalize a redistribution of electron density from SWCNTs to the electron-accepting **POM-pyr** to be responsible for the noted shift to lower energies. Examination of the fluorescence intensities (**Fig. 7**) prompts to approximately 90% quenching of the HiPco SWCNTs features. Regarding the electron accepting and electron donating features of **POM-pyr** and SWCNTs, respectively, we hypothesize that the fluorescence quenching is due to a non-radiative singlet excited state deactivation in the form of an electron transfer process from the photoexcited SWCNT to the POM with energies of equal or less than 1.2 eV (**Fig. 8**).[16,38] The relative excited state energies of SWCNTs and POMs were determined based on the long wavelength absorption and short wavelength fluorescence as ~ 1.2 and ~ 3.0 eV, respectively. These contradict, however, to the feasibility of an energy transfer, which would be thermodynamically uphill. Moreover, we have no particular evidence for an energy transfer between different SWCNTs. The latter is taken from the fact that the fluorescence of (10,2), (9,4), (8,6), (8,7), and (9,7) SWCNTs are equally quenched.

Electronic interactions in HiPco **SWCNT-POM** hybrids were corroborated by Raman experiments. Here, the most important SWCNT signatures which are, RBM (~ 300 cm^{-1}), D (~ 1300 cm^{-1}), G- (~1600 cm^{-1}), and 2D-modes (~2550 cm^{-1}),[28a] reveal upshifts in D_2O suspensions of HiPco **SWCNT-POM** with respect to HiPco SWCNT/SDBS as well as in the solid without evidencing loss in resonance. For example, the G and 2D modes of HiPco SWCNTs shift from 1590 ± 2 to 1592 ± 2 cm^{-1} and from 2548 ± 2 to 2552 ± 2 cm^{-1}, respectively (**Fig. 9**). This leaves no doubt that interactions are indeed operative between SWCNTs and **POM-pyr** but only in the excited state. Augmentation of electronic interactions in the ground state

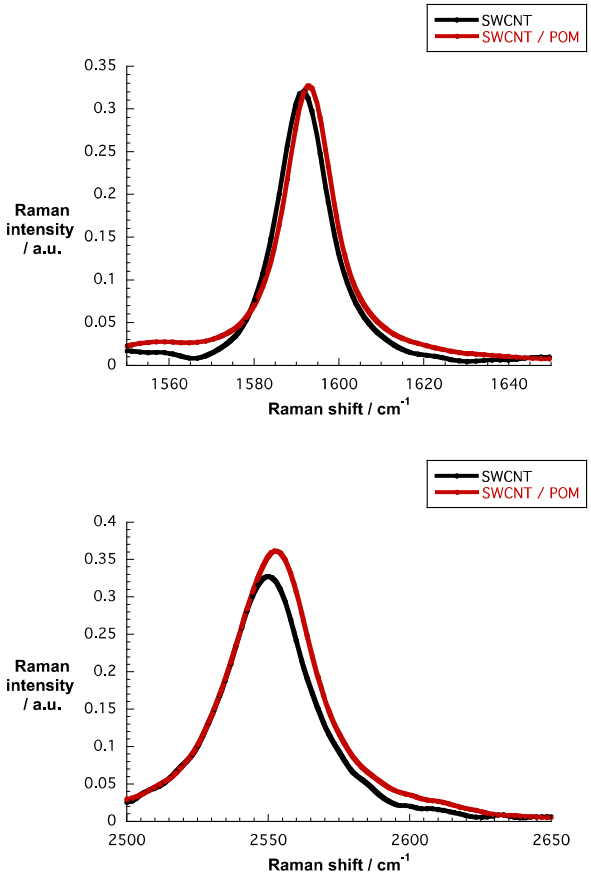

Figure 9. (*Top*) Raman spectra of SWCNT/SDBS (black spectrum) in D_2O suspension and **SWCNT-POM** (red spectrum) in DMF showing the G band. (*Bottom*) Raman spectra of SWCNT/ SDBS (black spectrum) in D_2O suspension and **SWCNT-POM** (red spectrum) in DMF showing the D* band. The spectra have been taken upon 1064 nm excitation.

through, for example, charge transfer is ruled out, since no additional features are superimposed on the G band.

To determine the dynamics of the ultrafast excited state deactivation in HiPco **SWCNT-POM** hybrids, which was inferred from the fluorescence assays (*vide supra*), we employed transient absorption spectroscopy. In reference experiments, photoexcitations of **POM-pyr** (**Fig. SI5**) and HiPco SWCNT/SDBS (**Fig. SI6**) were probed at 387 nm. For **POM-pyr**, centered excited states are generated instantaneously upon photoexcitation. The corresponding spectral characteristics include transient maxima at 525, 630, 700, 1130, and 1350 nm and are assigned to higher lying excited states. In line with this assignment is the fact that an overall short lifetime of 2 ± 0.2 ps transforms these into maxima at 515, 600, 920, 1090, and 1290 nm. From here, we note a biphasic decay. On one hand, after a short lifetime of around 75 ± 25 ps maxima are noted at 485, 535, 600, and 660 nm. The short lifetime is rationalized on the basis of strong spin-orbit couplings due to the presence of the metal centres and, in turn, correlates with the decay of the singlet excited state. On the other hand, a long lifetime of > 7500 ps, which relates to the correspondingly formed triplet excited state,

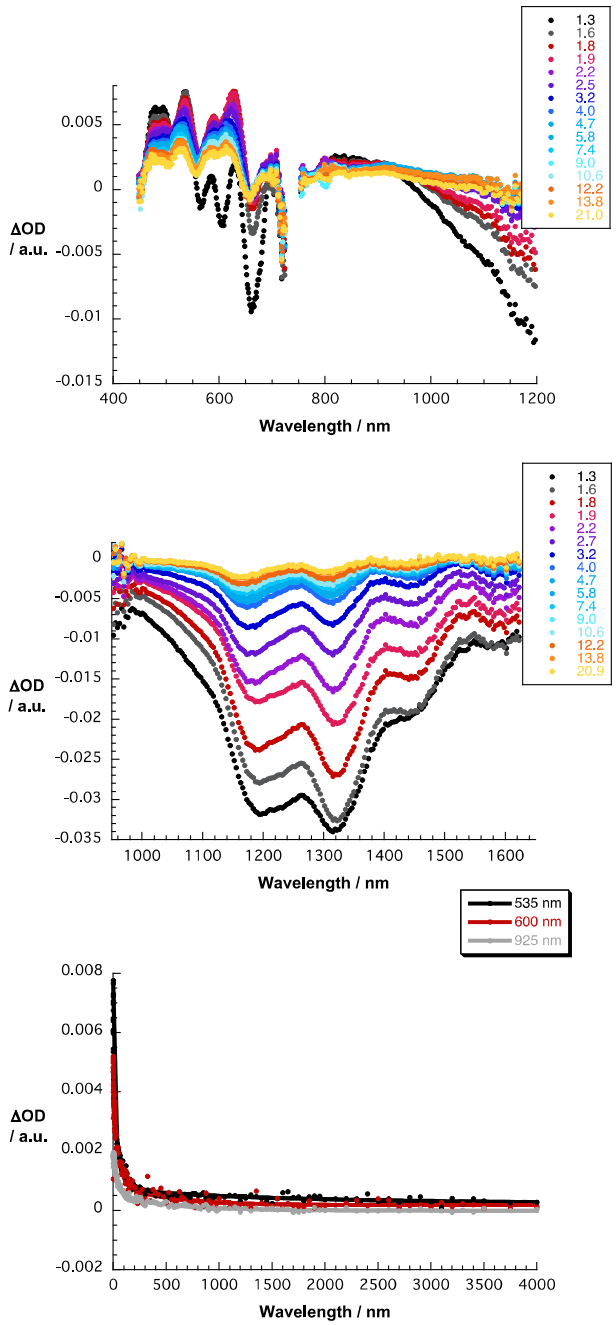

Figure 10 (*Top*) Differential absorption spectra (visible and near infrared) obtained upon femtosecond pump probe experiments (387 nm) of **SWCNT-POM** in DMF with time delays of 1.3 and 20.9 ps at room temperature. (*Centre*) Differential absorption spectra (extended near infrared) obtained upon femtosecond pump probe experiments (387 nm) of **SWCNT-POM** in DMF with time delays of 1.3 and 20.9 ps at room temperature. (*Bottom*) Time absorption profiles of the spectra shown in the upper part at 535 (black spectrum), 600 (red spectrum), and 925 nm (grey spectrum) monitoring the charge transfer.

renders this transient rather stable prior to undergoing a possible electron transfer. With respect to the HiPco SWCNT/SDBS, the baseline is replaced with a strong bleaching that dominates the differential absorption spectra throughout the visible and near-

infrared regions, where absorptive transitions of semiconducting SWCNTs appear, respectively (**Fig. SI6**). The major minima are seen at 975, 1190, 1325, and 1460 nm. Multiwavelength analyses of the bleaching characteristics in the near-infrared resulted in complex dynamics with two dominant lifetimes, namely 1.2 ± 0.2 and 520 ± 10 ps. Throughout these multiexponential decays the original absorption / baseline is quantitatively reinstated. Hereby, the polydisperse nature of HiPco SWCNTs evokes a superimposition of a series of bleaching features. The latter is correlated with individual SWCNTs that absorb in nearly the same energetic range.

When turning to the HiPco **SWCNT-POM** hybrids, conditions were chosen that guaranteed stable SWCNT suspensions. Interesting is the fact, that the instantaneous bleaching follows the trend seen in the absorption assays. To this end, minima and shoulders in the differential absorption spectra at 565, 605, 660, 995, 1193, 1320, 1445, and 1585 nm correlate well with the maxima and shoulders found in the absorption spectra at 560, 605, 660, 1194, 1320, 1445, and 1585 nm and, in turn, are SWCNT centered (**Fig. 10**). In addition, maxima are noted at 475, 495, 535 and 820 nm. In fact, lifetimes of 25 ± 4 and 1600 ± 100 ps were derived from a multiwavelength analysis, which strongly evoke charge separation and charge recombination. Evidence for the charge transfer hypothesis, that is, charge separation and charge recombination, was learnt from fine structured maxima in the visible and the near-infrared at 475, 525, 585, 615, 690, 1255, 1375, and 1525 nm, which feature weak positive differential absorption changes. In addition, broad maxima are discernable in the 700 to 1200 nm range, in general, and the 850 nm maximum, in particular. In agreement with previous spectroelectrochemical experiments, we assign the earlier to oxidized SWCNTs, while the latter bear great resemblance with reduced **POM-pyr**.

Experimental

Synthesis.

General Synthetic Remarks. Elicarb Single Walled Nanotubes (SWCNTs) were purchased from Thomas Swan Co. LTD. and HiPco SWCNTs were purchased from Unidym Inc. The samples were filtered employing a vacuum filter funnel pore size 3, and nylon membrane filters (ø 0.2 µm pore size). The ultrasound conditions were achieved with a Brandson 5510E-MT operating a 135 W.

Synthesis of POM-pyr. POM-pyr was synthesized following the reported procedure.[31]

Synthesis of SWCNT-POM hybrid. 6 mg of SWCNTs were dispersed in 24 mL of DMF by applying ultrasounds during 30 minutes (Brandsonic 5510). Afterwards, 8mg of POM-pyr were added to the above mixture and the slurry stirred during 4 hours. Then, the mixture was left to settle down during one night, and the nanotubes were washed by dispersing them first with DMF and secondly with acetonitrile with the aid of ultrasounds. Finally, SWCNT-POM were isolated by filtering through a nylon membrane filter (0.2 µm pore size) and washing them with acetonitrile and with ethanol.

Physical characterization.

HR-TEM images were obtained using a TECNAI G2 F20 microscope. Field Emission Gun (FEG)200 kV. Aberration corrected HAADF and BF-STEM images were obtained in a JEOL ARM 200F microscope operating at 80 keV, equipped with CEOS spherical aberration correctors both for probe and image formation. Spherical aberration coefficients C3 is almost 0 mm and C5 is around 5 mm. An objective aperture has been used, and the convergence semiangle is 22 mrad . Inner and outer annular detector angles for HAADF STEM are about 50 and 200 mrad, respectively. Thermogravimetric analysis was carried out with a Mettler Toledo TGA/SDTA 851 apparatus in the 25-800ºC temperature range under air aotmosphere and at 10K min^{-1} scan rate. X-ray photoelectron spectroscopy (XPS) measurements were performed in an ultra-high vacuum system ESCALAB210 (base pressure $1.0x10^{-10}$ mbar) from Thermo VG Scientific. Photoelectrons were excited by using the Mg-Kα line (1253.6 eV). All spectra have been referred to the Fermi level.

Photophysical Measurements. Steady-state UV/vis/NIR absorption spectroscopy was performed on a Cary 5000 spectrometer (Varian). Transient absorption spectroscopy was performed with 387 nm laser pulses from an amplified Ti/sapphire laser system (ModelCPA2101, Clark-MXR Inc.; output: 775 nm, 1 kHz, and 150 fs pulse width) in the TAPPS (transient absorption pump/probe system) Helios from Ultrafast Systems with 200 nJ laser energy. Steady-state fluorescence spectra were taken from samples with a with a FluoroLog3 spectrometer (Horiba) with a IGA Symphony (5121 1 µm) detector in the NIR detection range. The Raman spectra were recorded with a FT-Raman spectrometer RFS100 (Bruker).

Spectroelectrochemical measurements. All experiments were carried out in deoxygenated DMF purchased from Sigma Aldrich with 0.1 M or 0.2 M $TBAPF_6$ (Sigma Aldrich) as supporting electrolyte. All chemicals were used without further purification.

For spectroelectrochemical measurements, a quartz cell with an optical pathway of 1 mm or a home made three neck cell was used in combination with an three electrode setup. A platinum gauze served as working electrode, a platinum wire as counter electrode and a $Ag/AgNO_3$ in Acetonitrile was chosen as reference electrode. In case of the three neck cell, $Ag/AgNO_3$ was replaced by a silver wire serving as quasi reference electrode. Changes in Absorption were monitored either by a Speccord S600 (Analytik Jena) spectrometer or a Cary 5000 spectrometer (Varian)

Potentials were applied and controlled by means of an PGSTAT 101 potentiostat from Methrom© and the corresponding software NOVA 1.6©.

Conclusions

Pyrene-appended Dawson-Wells-type polyoxometalates have been successfully immobilized onto SWCNTs by means of non-covalent forces. Non-covalent functionalization relies on the presence of π-π interactions between the sidewalls of SWCNTs and the π-conjugated pyrene, which afford stable suspensions of strongly coupled **SWCNT-POM** hybrids. Formation of the hybrids was confirmed with high-resolution electron microscopy, XPS experiments, and thermogravimetric analysis. From the latter we estimate a loading of at least 1 **POM-pyr** per 4600 carbon atoms, which corresponds to a 10 % coverage. Our photophysical studies confirm electron transfer from the photoexcited SWCNTs to the grafted polyoxometalate. The

dynamics of the process, studied by transient absorption spectroscopy, reveal the appearance of metastable characteristics of oxidized SWCNTs and reduced **POM-pyr**. This is quite remarkable, as both components, **POM-pyr** and SWCNTs are commonly used as electron acceptors. Our results demonstrate the potential of SWCNTs and **POM-pyr**s for the design of photoactive molecular devices, which alongside the ability of POMs to undergo multiple reduction reactions with minor structural changes, qualify them as promising electron reservoirs for the design of advanced dyads.

Acknowledgements

Financial support from the EU (Projects COST Action CM1203 PoCHeMoN, ELFOS and ERC Advanced Grant SPINMOL), the Spanish Ministerio de Economía y Competitividad (Projects MAT2011-22785), and the Generalitat Valenciana (Prometeo Program) are gratefully acknowledged. AMR and SIM acknowledge the support from the Spanish MINECO (projects TEC2011-29120-C05-03 and Consolider Ingenio 2010 CSD2009-00013) and the Junta de Andalucía (PAI research group TEP-946 INNANOMAT), and also to JEOL company for the use of a double-corrected aberration-corrected ARM electron microscope. C.M.-G. thanks the Spanish MINECO for a Ramón y Cajal Fellowship (RYC-2012-10894).

Notes and references

[*,a] Universidad de Valencia (ICMol), Catedrático José Beltrán-2, 46980, Paterna (Spain)
E-mail: eugenio.coronado@uv.es, carlosmartigastaldo@gmail.com
[*,b] Institut Parisien de Chimie Moléculaire, Sorbonne Universités UPMC Univ Paris 06, UMR CNRS 7201, Université Pierre et Marie Curie, UPMC Univ Paris 06, 4 place Jussieu, Case 42, 75252, Paris Cedex 05, France.
E-mail: anna.proust@upmc.fr
‡ Current address: Organisch-Chemisches Institut, Im Neuenheimer Feld 270, 69129, Heidelberg, Germany.
[*,c] Friedrich-Alexander-Universität Erlangen-Nürnberg, Department Chemie und Pharmazie und Interdisziplinäres Zentrum für Molekulare Materialien, Egerlandstrasse 3, 91058, Erlangen, Germany.
E-mail: dirk.guldi@fau.de
[d] Departamento de Ciencia de los Materiales e I.M. y Q.I., Facultad de Ciencias, Universidad de Cádiz, Campus Río San Pedro, s/n, 11510, Puerto Real, Cádiz (Spain)

†Electronic Supplementary Information (ESI) available: Thermogravimetric Analysis, additional HRTEM, HAADF-STEM and BF-STEM images, and differential absorption spectra. See DOI: 10.1039/b000000x/

††Abbreviations. POMs, Polyoxometalates; SWCNTs, Single Wall Carbon Nanotubes; FETs, Field-Effect Transistors; Pyr, Pyrene; TGA, Thermogravimetric Analysis; EDS, Energy-Dispersive X-ray Spectroscopy; HRTEM, High Resolution Transmission Electron Microscopy; HAADF-STEM, High-Angle Annular Dark-Field Scanning-Transmission Electron Microscopy; BF, Bright Field; XPS, X-Ray Photoelectron Spectroscopy; BEs, Binding Energies.

1 D. Eder, *Chem. Rev.,* 2010, **110**, 1348.
2 R.H. Baughman, A.A. Zakhidov, W.A. de Heer, *Science,* 2002, **297**, 787.
3 M. Urdampilleta, S. Klyatskaya, J.-P. Cleuziou, M. Ruben, W. Wernsdorfer, *Nature Mater.,* 2011, **10**, 502; L. Bogani, W. Wernsdorfer, *Inorg. Chim. Acta,* 2008, **361**, 3807.
4 V. Sgobba, D.M. Guldi, *Chem. Soc. Rev,*. 2009, **38**, 165.
5 Y. Liang, Y. Li, H. Wang, H. Dai, *J. Am. Chem. Soc.,* 2013, **135**, 2013; F. Li, B. Zhang, X. Li, Y. Jiang, L. Chen, Y. Li, L. Sun, *Angewandte Chemie,* 2011, **123**, 12484.
6 C. Dekker, S.J. Tans, A.R.M. Verschueren, *Nature,* 1998, **393**, 49.
7 J. Kong, N.R. Franklin, C. Zhou, M.G. Chapline, S. Peng, K. Cho, H Dai, *Science*, 2000, **287**, 622; E. Katz, I. Willner, *ChemPhysChem,* 2004, **5**, 1084.
8 D.-L. Long, E. Burkholder, L. Cronin, *Chem. Soc. Rev.,* 2007, **36**, 105.
9 M.A. AlDamen, J.M. Clemente-Juan, E. Coronado, C. Martí-Gastaldo, A. Gaita-Ariño, *J. Am. Chem. Soc.,* 2008, **130**, 8874.
10 L. Bogani, W. Wernsdorfer, *Nature Mater.,* 2008, **7**, 179. J.M. Clemente-Juan, E. Coronado, A. Gaita-Ariño, *Chem. Soc. Rev.,* 2012, **41**, 7464.
11 A. Sartorel, M. Carraro, G. Scorrano, R. De Zorzi, S. Geremia, N.D. McDaniel, S. Bernhard, M. Bonchio, *J. Am. Chem. Soc.,* 2008, **130**, 5006; Y.V. Geletii, B. Botar, P. Kögerler, D.A. Hillesheim, D.G. Musaev, C.L. Hill, *Angew. Chem. Int. Ed.,* 2008, **120**, 3960; S. Goberna-Ferrón, L. Vigara, J. Soriano-López, J.R.G Mascarós, *Inorg. Chem.,* 2012, **51**, 11707; H. Lv, Y.V. Geletii, C. Zhao, J.W. Vickers, G. Zhu, Z. Luo, J. Song, T. Lian, D.G. Musaev, C.L. Hill, *Chem. Soc. Rev.,* 2012, **41**, 7572.
12 D. Pan, J. Chen, W. Tao, L. Nie, S. Yao, *Langmuir,* 2006, **22**, 5872.
13 A. Giusti, G. Charron, S. Mazerat, J.D. Compain, P. Mialane, A. Dolbecq, E. Rivière, W. Wernsdorfer, R. Ngo Biboum, B. Keita, *Angew. Chem. Int. Ed.,* 2009, **121**, 5049; G. Charron, A. Giusti, S. Mazerat, P. Mialane, A. Gloter, F. Miserque, B. Keita, L. Nadjo, A. Filoramo, E. Rivière, *Nanoscale,* 2010, **2**, 139.
14 F.M. Toma, A. Sartorel, M. Iurlo, M. Carraro, P. Parisse, C. Maccato, S. Rapino, B.R. Gonzalez, H. Amenitsch, T. Da Ros, *Nature Chem.,* 2010, **2**, 826.
15 N. Kawasaki, H. Wang, R. Nakanishi, S. Hamanaka, R. Kitaura, H. Shinohara, T. Yokoyama, H. Yoshikawa, K. Awaga, *Angew. Chem. Int. Ed.,* 2011, **50**, 3471; H. Wang, N. Kawasaki, T. Yokoyama, H. Yoshikawa, and K. Awaga, *Dalton Trans.*, 2012, **41**, 9863.
16 B. Matt, C. Coudret, C.Viala, D. Jouvenot, F. Loiseau, G. Izzet, A. Proust, *Inorg. Chem.,* 2011, **50**, 7761; B. Matt, X. Xiang, A.L. Kaledin, N. Han, J. Moussa, H. Amouri, S. Alves, C.L. Hill, T. Lian, D.G. Musaev, G. Izzet, A. Proust, *Chem. Sci.,* 2013, ***4***, 1737; B. Matt, J. Fize, J. Moussa, H. Amouri, A. Pereira, V. Artero, G. Izzet, A. Proust, *Energy Environ. Sci.,* 2013, **6**, 1504.
17 G. Izzet, M. Ménand, B. Matt, S. Renaudineau, L.-M. Chamoreau, M. Sollogoub, A. Proust, *Angew. Chem. Int. Ed.,* 2012, **51**, 487.
18 C. Rinfray, G. Izzet, J. Pinson, S. Gam Derouich, J.-J. Ganem, C. Combellas, F. Kanoufi, A. Proust, *Chem. Eur. J.,* 2013, **19**, 13838.
19 V. Duffort, R. Thouvenot, C. Afonso, G. Izzet, A. Proust, *Chem. Commun.,* 2009, 6062. M.M. Lorion, B. Matt, S. Alves, A. Proust, G. Poli, J. Oble, G. Izzet, *Chem. Eur. J.,* 2013, **19**, 12607.
20 A. Proust, B. Matt, R. Villanneau, G. Guillemot, P. Gouzerh, G. Izzet, *Chem. Soc. Rev.,* 2012, **41**, 7605.
21 M. Herranz, N. Martín, S. Campidelli, M. Prato, G. Brehm, D.M. Guldi, *Angew. Chem. Int. Ed.,* 2006, **118**, 4590. B. Ballesteros, G. de L. Torre, C. Ehli, G.M.A. Rahman, F. Agulló-Rueda, D.M. Guldi, T. Torres, *J. Am. Chem. Soc.,* 2007, **129**, 5061. C. Oelsner, M.A. Herrero, C. Ehli, M. Prato, D.M. Guldi, *J. Am. Chem. Soc.,* 2011, **133**, 18696. C. Bosch-Navarro, E. Coronado, C. Martí-Gastaldo, B. Rodríguez-González, L.M. Liz-Marzán, *Adv. Func. Mater.,* 2012, **22**, 979.
22 E.W. McQueen, J.I. Goldsmith, *J. Am. Chem. Soc.,* 2009, **131**, 17554.
23 S. Kyatskaya, J.R.G. Mascarós, L. Bogani, F. Hennrich, M. Kappes, W. Wernsdorfer, M. Ruben, *J. Am. Chem. Soc.,* 2009, **131**, 15143. L. Bogani, C. Danieli, E. Biavardi, N. Bendiab, A.-L. Barra, E. Dalcanale, W. Wernsdorfer, A. Cornia, *Angew. Chem. Int. Ed.,* 2009,

121, 746. M. Ganzhorn, S. Klyatskaya, M. Ruben, W. Wernsdorfer, *ACS Nano,* 2013, **7**, 6225.
24 J. Bartelmess, C. Ehli, J.-J. Cid, M. García-Iglesias, P. Vázquez, T. Torres, D.M. Guldi, *J. Mater. Chem.,* 2011, **21**, 8014. M. Ince, J. Bartelmess, D. Kiessling, K. Dirian, M.V. Martínez-Díaz, T. Torres, D.M. Guldi, *Chem. Sci.,* 2012, **3**, 1472.
25 C. Schulz Drost, V. Sgobba, C. Gerhards, S. Leubner, R.M. Krick Calderon, A. Ruland, D.M. Guldi, *Angew. Chem. Int. Ed.,* 2010, **49**, 6425. L. Hu, Y.-L. Zhao, K. Ryu, C. Zhou, J.F. Stoddart, G. Grüner, *Adv. Mater.,* 2008, **20**, 939.
26 H. Xin, A.T. Woolley, *J. Am. Chem. Soc.,* 2003, **125**, 8710.
27 C. Romero-Nieto, R. García, M.A. Herranz, C. Ehli, M. Ruppert, A. Hirsch, D.M. Guldi, N. Martin, *J. Am. Chem. Soc.,* 2012, **134**, 9183.
28 D. Ma, L. Liang, W. Chen, H. Liu, Y.-F. Song, *Adv. Funct. Mater.,* 2013, **23**, 6100. G. Modugno, Z. Syrgiannis, A. Bonasera, M. Carraro, G. Giancane, L. Valli, M. Bonchio, M. Prato, *Chem. Commun.,* 2014, DOI 10.1039/c3cc49725a.
29 B. Dawson, *Acta Cryst.,* 1953, **6**, 113.
30 D.-L. Long, P. Kögerler, A.D.C. Parenty, J. Fielden, L. Cronin, *Angew. Chem. Int. Ed.,* 2006, **45**, 4798. L. Vilà-Nadal, K. Peuntinger, C. Busche, J. Yan, D. Lüders, D.-L. Long, J.M. Poblet, D.M. Guldi, L. Cronin, *Angew. Chem. Int. Ed.,* 2013, **52**, 9695.
31 B. Matt, S. Renaudineau, L.M. Chamoreau, C. Afonso, G. Izzet, A. Proust, *J. Org. Chem.,* 2011, **76**, 3107.
32 D. Bom, R. Andrews, D. Jacques, J. Anthony, B. Chen, M.S. Meier, J.P. Selegue, *Nano Lett.,* 2002, **2**, 615.
33 X. Zhang, L. Hou, A. Cnossen, A.C. Coleman, O. Ivashenko, P. Rudolf, B.J. van Wees, W.R. Browne, B.L. Feringa, *Chem. Eur. J.*, 2011, **17**, 8957.
34 R. Liu, S. Li, X. Yu, G. Zhang, S. Zhang, J. Yao, L. Zhi, *J. Mater. Chem..,* 2012, **22**, 3319.
35 Changes due to differences in the environment are, however, ruled out based on the similarities in absorption features.
37 H. Kataura, Y. Kumazawa, Y. Maniwa, I. Umezu, S. Suzuki, Y. Ontsuka, Y. Achiba, *Synt. Met.*, 1999, **103**, 2555.
38 C. Romero-Nieto, R. Garcia, M. Angeles-Herranz, L. Rodriguez-Perez, M. Sanchez-Navarro, J. Rojo, N. Martin, D.M.Guldi, *Angew. Chem. Int. Ed.*, 2013, **52**, 10216.